

Imaging of Spatiotemporal Coincident States by Dynamic Optical Tomography

Harry L. Graber¹, Yaling Pei², Randall L. Barbour^{1,2}

1. SUNY Downstate Medical Center, 450 Clarkson Avenue, Brooklyn, NY 11203

2. NIRx Medical Technologies Corp., 15 Cherry Lane, Glen Head, NY 11545

ABSTRACT

The utility of optical tomography as a static imaging modality is limited by its intrinsically low spatial resolution and quantitative accuracy. When applied to dynamic measurements, however, optical imaging methods have the potential to assess tissue function as revealed by temporal variations in tissue optical properties. These variations are a consequence of vascular hemodynamic processes, which are known to exhibit considerable spatiotemporal heterogeneity. In this report we provide evidence, from simulation, that complex dynamic behavior in optical coefficients occurring in localized regions in highly scattering media can be accurately characterized by the method of dynamic optical tomography, even in the limiting case of spatiotemporally coincident behavior.

Keywords: Dynamic optical tomography, Physiological dynamics, Physiological oscillations, Inverse problem, Cross-talk and non-uniqueness

1. INTRODUCTION

Assessment of tissue function by noninvasive methods is playing an increasingly important role in the detection and management of disease processes. One measure of significance is the monitoring of hemoglobin states. These can be studied continuously and noninvasively with near infrared (NIR) optical methods. Many groups are attempting to apply these methods in a tomographic imaging mode for the purpose of studying large tissue structures. Thus far, however, such efforts have met with limited success. One concern is the spatial resolution, which most investigators report as being on the order of 0.5 cm at best. How much of this is due to fundamental limits attributable to scattering, and how much to limits in methodology, is unclear. Regardless, given the resolution of alternative imaging methods, the practical utility of spatial maps having such resolution seem limited. It is our view, however, that the real value of imaging large tissue structures with NIR light lies in having superior performance not in the spatial domain, but rather in the time domain.

Measures that provide information regarding the temporal properties of hemoglobin states in tissue (*i.e.*, blood volume, blood oxygenation) are commonly performed and have substantial value. For thin structures (*e.g.*, fingers), optical methods in the form of pulse oximetry and photoplethysmography are used to measure arterial oxygenation levels and blood volume changes, respectively. For large tissues, the latter is often measured using pneumoplethysmographic methods in the form of pulse volume recording. In each case, the methodology employed provides a spatially integrated, time-varying signal.

A key value to performing repeated, rapid measurements using NIR optical methods is that one can isolate signals unique to the vascular compartment. Significantly, features of the vascular rhythms, which include the cardiac (~1 Hz – ~2 Hz), respiratory (~0.1 Hz – ~0.5 Hz) and vasomotor (~0.04 Hz – ~0.15 Hz) frequency ranges, are known to reflect critical physiological functions and often serve as markers for disease. For instance, a reduced amplitude in the cardiac frequency band, when observed distal to areas having more normal values in pulse volume recordings, is a reliable indicator of arterial stenosis between the two measuring sites. In situations of this type, we believe that the ability to localize such events on the basis of their *temporal signatures*, without the need for contrast agents, and with a spatial resolution of that currently achievable by optical tomography, could have substantial practical value. In addition to pathologies associated with the principal arteries, it is likely that many other practical applications could be found from studies focused on the venous and microcirculatory branches of the vascular tree. In fact, features attributable to the principal structures of the vascular tree are readily identifiable owing to their distinct temporal properties. For instance, detection of a beat frequency in the periphery equal to the rate of ventricular contraction can be reliably taken as originating from arterial structures. Similar associations are well known between the respiratory frequency and venous structures, and vasomotor frequencies and the microvessels.

The existence of distinct frequency ranges in the vascular response, the deep penetrating power of NIR photons, and the relative homogeneity of chromophores that absorb light at these wavelengths in tissue is a most useful fortuitous combination. Whereas the value of optical- or hemodynamic-parameter maps may be limited as a consequence of their modest spatial resolution, it is our view that similar maps that encode temporal signatures, which serve to define distinct functional properties of the vasculature and its interaction with the surrounding tissues, will likely have substantial value. It is worth emphasizing that this information is obtainable without the use of contrast agents. The contrast mechanism is the natural temporal variability of the hemoglobin signal itself.

Recently we have begun to explore this promising territory. Our approach comprises three principal efforts. First, we recognize the need to have available a well-engineered, yet flexible, data collection platform suitable for examining the temporal variability of vasculature properties in large tissue structures. The accompanying report by Schmitz *et al.*¹ summarizes our latest work in this area. Second, we have sought to improve on the stability and speed of the numerical methods used for image reconstruction. The report by Pei *et al.*² describes a new algorithm we have developed that apparently is effective in minimizing inter-parameter cross-talk using DC measurement data. Third, we have focused our attention on characterizing the accuracy with which temporal information attributable to dynamic processes can be identified in reconstructed spatial maps obtained using the experimental and numerical methods we have developed.³⁻⁶

Motivating our design of these studies has been the considerable literature indicating that particular forms of temporal variability may have significant diagnostic and therapeutic implications. Specifically, we are referring to dynamic states that governed by chaotic nonlinear processes. This behavior is characterized by the property of “sensitive dependence on initial conditions,”⁷ and its occurrence in biology appears pervasive. It is believed that this behavior confers an adaptive advantage, as it allows for large effects with the expenditure of only a small amount of energy. This property, widely observed in natural systems, has become known as the “butterfly effect,” in keeping with the idea that the “flap of a butterfly’s wing in Brazil” could, at least in theory, “cause a tornado in Texas.”⁸

The occurrence of chaotic phenomena in biology may also have important implications for therapy. Some years ago, Glass and Mackey proposed that many diseases are characterized by abnormal temporal organization in the control of normal physiological processes, and they coined the term “dynamical diseases” to refer to conditions of this type.⁹ It has been suggested that such behaviors can have important implications for the approach taken in many pharmacological interventions. The idea here is that rather than basing drug administration regimens simply on the goal of achieving a target steady-state concentration, the time course of administration may also be critical. For example, as pointed out by Griffith,⁸ the cardiovascular response of two patients to administration of a drug such as verapamil may be very different, and may even differ in the same patient depending the day it is administered.

One model of dynamic behavior we have considered is the occurrence of spatiotemporally coincident behavior. This refers to states wherein two or more time-varying processes are occurring at the same time and location. Certainly, such behavior can be expected in tissue. For instance, temporal fluctuations in tissue blood volume at any one site need not parallel that of blood oxygenation. Similarly, the variability in the tissue optical absorption coefficient need not follow changes in light scattering.

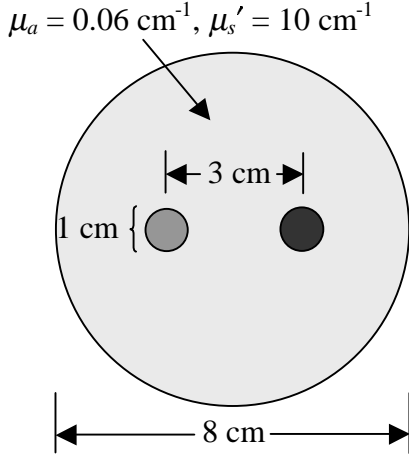
In this report we have explored our ability to accurately characterize complex dynamic behavior in dense scattering media as a model of tissue, in the limiting case in which two different processes are spatially and temporally coincident. In particular, we have sought a further test of the fidelity with which the normalized-constraint method reported by Pei *et al.* (see accompanying report)² can simultaneously distinguish perturbations in absorption and diffusion coefficients when both exhibit different complex temporally varying behaviors. Our test model considered two included objects, each of which had two distinct complex time-varying functions assigned to it, one corresponding to its absorption coefficient and the other to its scattering coefficient. Results obtained add to the accumulating evidence that the method of dynamic optical tomography is capable of accurately characterizing complex dynamic states in highly scattering media.

2. METHODS

2.1 Spatiotemporal properties of target medium

The target medium, as shown in Figure 1, is a geometrically simple 2-D structure consisting of an 8-cm circle with two embedded 1-cm diameter inclusions. The absorption (μ_a) and reduced scattering (μ_s') coefficients of the light grey background in the Figure were static, while four time-varying functions — $\mu_a(l,t)$, $\mu_s'(l,t)$, $\mu_a(r,t)$, and $\mu_s'(r,t)$, where l and r respectively denote the left-hand (dark grey region in Figure 1) and right-hand (black region in Figure 1) — were assigned to the optical coefficients in the inclusions. That is, four different aperiodic fluctuations were present in the medium

Figure 1 Dimensions and geometry of target medium



simultaneously, with two of the four spatially coincident in each inclusion. The static background values of μ_a and μ_s' are indicated in Figure 1, while the ranges of coefficient values and the types of temporal fluctuation modeled are specified in Table 1, and plots, rescaled to range from -1 to +1, showing the first two hundred points of the four time courses are shown in Figure 2. The ranges indicated for μ_a and μ_s' in Table 1 represent 20% fluctuations about mean values of 0.12 cm^{-1} and 15 cm^{-1} , respectively. The quasiperiodic time series for $\mu_a(l,t)$ was generated by adding two sinusoidal functions with incommensurate frequencies,¹⁰ then computing one thousand function values at regular spaced time intervals. Chaotic time series were generated for $\mu_s'(l,t)$ and $\mu_a(r,t)$ by assigning randomly generated initial values to the Hénon equation¹¹ and computing one thousand successive iterations. While the same equation was used for both time series, by choosing different initial values the two chaotic time series generated are uncorrelated. The stochastic time series was generated by drawing one thousand independent samples from a random variable uniformly distributed between -1 and +1.

Table 1 Properties of temporal fluctuations assigned to inclusions' optical coefficients

μ_a			μ_s'		
Range (cm^{-1})	Dynamics		Range (cm^{-1})	Dynamics	
	Left	Right		Left	Right
0.096 – 0.144	Quasiperiodic	Chaotic	12 – 18	Chaotic	Stochastic

2.2 Detector data generation

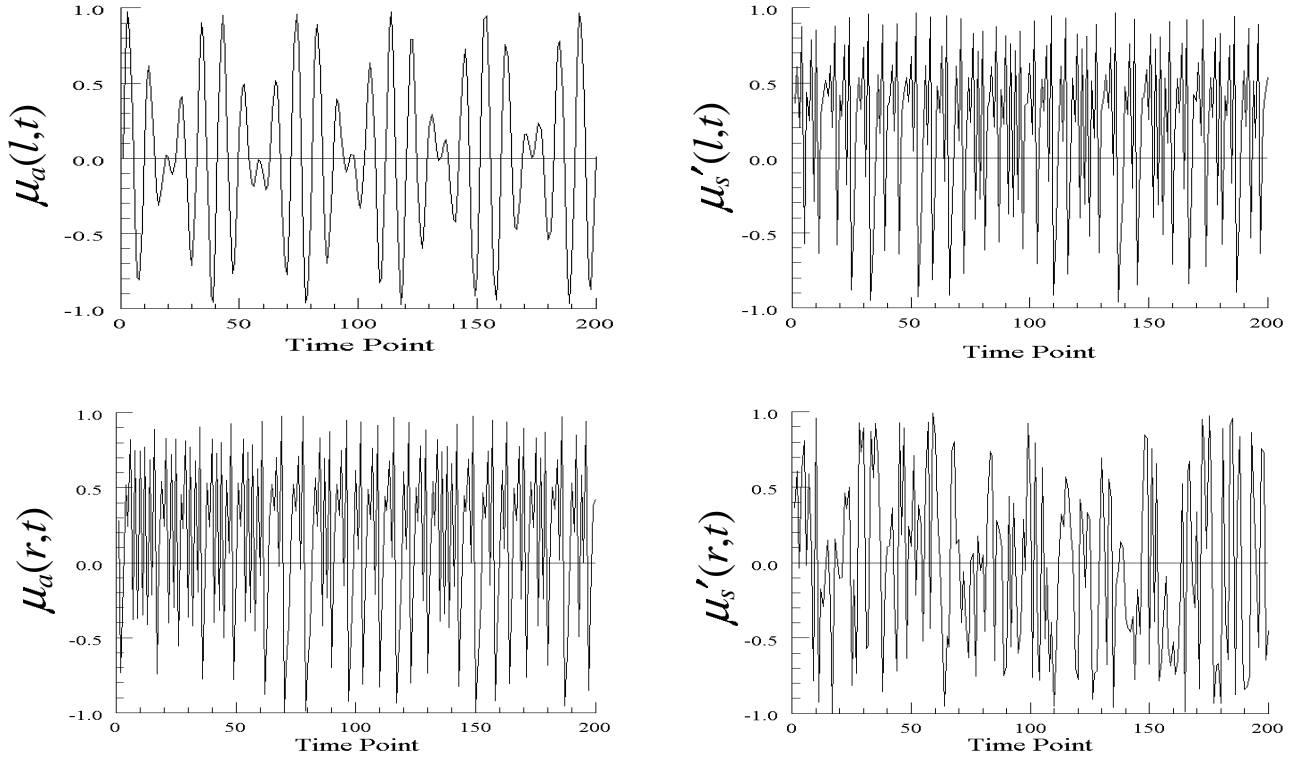
Tomographic data for the simulated tissue models were acquired by using the finite element method to solve the diffusion equation with Dirichlet boundary conditions for a DC source.^{2,12} For a spatial domain Λ with boundary $\partial\Lambda$, this is represented by the expression

$$\nabla \cdot [D(\mathbf{r})\nabla\phi(\mathbf{r})] - \mu_a(\mathbf{r})\phi(\mathbf{r}) = -\delta(\mathbf{r} - \mathbf{r}_s), \quad \mathbf{r} \in \Lambda, \quad (1)$$

where $\phi(\mathbf{r})$ is the photon intensity at position \mathbf{r} , \mathbf{r}_s is the position of a DC point source, and $D(\mathbf{r})$ and $\mu_a(\mathbf{r})$ are the position-dependent diffusion and absorption coefficients, respectively. Here the definition used for the diffusion coefficient was $D(\mathbf{r}) = 1/\{3[\mu_a(\mathbf{r}) + \mu_s'(\mathbf{r})]\}$, where $\mu_s'(\mathbf{r})$ is the position-dependent reduced scattering coefficient. (This same definition of D will subsequently be applied to the optical coefficients assigned to the target medium). Forward-problem solutions were computed for each of six sources positioned about the target at 60° intervals, with each source located at a depth of 2 mm in from the extended boundary (*i.e.*, within the strip lying between the physical and extended boundaries).¹² Intensity values at eighteen locations, at the same depth as the sources but spaced at 20° intervals, were used as detector readings. Imaging operators were computed, in the manner described in Ref. 13, for each of the resulting 108 source/detector pairs. Sets of detector readings were computed for each of the one thousand values of the time-varying optical coefficients in the target's inclusions. A single set of imaging operators, computed for a 8-cm-diameter homogeneous medium whose properties are equal to those of the static region of the target, was used for all inverse problem computations.

2.3 Image reconstruction procedures

The optical inverse formulation was based on the normalized difference method,² in which the equation that we solve has the form

Figure 2

Legend Time series (rescaled to range from -1 to +1) assigned to the optical coefficients of the target medium's inclusions.

$$\mathbf{W}_r \cdot \delta \mathbf{x} = \delta \mathbf{I}_r, \quad (2)$$

where $\delta \mathbf{x}$ is the vector of differences between the optical properties (*e.g.*, absorption and scattering coefficients) of a target (measured) and a “background” medium, \mathbf{W}_r is the weight matrix describing the influence that each voxel or element has on the surface detectors for the selected reference medium, and $\delta \mathbf{I}_r$ represents a normalized difference between detector readings obtained from the target in two distinct states. The normalized difference is defined by

$$(\delta \mathbf{I}_r)_i = \left(\frac{I_i - (\mathbf{I}_0)_i}{(\mathbf{I}_0)_i} \right) (\mathbf{I}_r)_i, \quad (3)$$

where \mathbf{I}_r is the computed detector readings corresponding to a selected reference medium, and \mathbf{I} and \mathbf{I}_0 represent two sets of measured data (*e.g.*, background *vs.* target, or time-averaged mean *vs.* a specific time point, *etc.*).

Two sets of image reconstructions were carried out on the detector data time series. In one of these a conjugate gradient descent (CGD) algorithm was used to compute numerical solutions to the modified perturbation equation (Eq. (2)), without imposition of any constraints or weight–matrix scaling. In the other, the CGD algorithm was employed along with the constraints–plus–scaling procedure that is more fully described in an accompanying report.² For convenience, in this report we refer to these two variants as, respectively, the normalized difference and the normalized–constraint CGD methods.

2.4 Quantitative assessment of temporal accuracy and inter–parameter cross–talk

An important feature we are interested in examining is the accuracy with which temporal variations in the optical coefficient values can be recovered in the limiting case of complex coincident behaviors. Such activity can be expected to occur throughout tissue *in vivo*, for instance, as a consequence of the known spatiotemporal heterogeneity in the vascular response. In an accompanying report by Pei *et al.*,² we describe a new method for image recovery that provides for improved separation of the absorption and scattering properties. Given the many factors that can influence reconstruction results, simply identifying improved isolation of the recovered absorption and scattering properties does not imply that similar results can be obtained in recovering the true temporal behavior in the coefficient values. For instance, should the amount of inter–

parameter cross-talk depend strongly on the ratio of the perturbations in the absorption and scattering coefficients, then apparently good qualitative isolation of the coefficients may be possible, but details of the associated temporal function could be severely corrupted.

To test this, we have quantified the accuracy with which various measures of temporal behavior corresponding to that introduced into the test objects are recovered. One convenient measure we have previously adopted is to generate a geometrical representation of the recovered time series corresponding to pixel data.⁴ This series is produced by plotting the variation in the recovered coefficient value in a selected pixel as a function of time, using the method of delays¹⁴ to produce a pseudo-state-space map. In the parlance of nonlinear dynamics studies, such a map forms an “attractor,” which often have shapes or forms that are “strange” in appearance, reflecting the presence of complex dynamic processes. These measures, while providing a simple and useful means of detecting particular types of complex functions, do not reveal the quantitative similarity between a test and recovered function.

Measures of correlation are frequently used to quantify the similarity of functions. For our case we have assessed the degree to which the recovered parameters are *temporally* accurate by computing the correlation coefficient (ρ), for individual pixels, between reconstructed μ_a time series and the functions used as models of time-varying μ_a and D in the same location. Ideally, in any given pixel the correlation between the target and image μ_a time series would be unity, while that between the target D and image μ_a would be zero. A finding of significant nonzero correlation in the latter case is indicative of inter-parameter cross-talk.

To assess the accuracy with which the recovered temporal behaviors coincide with the actual target locations, spatial maps of covariance (σ_{xy}) values between the object functions and the recovered pixel time series were computed. Covariance is the appropriate measure of the degree to which a recovered temporal behavior is *spatially* accurate because, unlike the correlation, the (absolute value of the) covariance between two time-varying functions is large only if both functions evolve similarly in time *and* they both have large-amplitude fluctuations. For these computations, the ideal result would be that the reconstructed $\mu_a(t)$ in pixels lying within the left- and right-hand inclusions, and only these pixels, show significant covariance with $\mu_a(l,t)$ and $\mu_a(r,t)$, respectively. At the same time, the reconstructed $\mu_a(t)$ should not significantly co-vary with either $D(l,t)$ or $D(r,t)$, in any region of the reconstructed images.

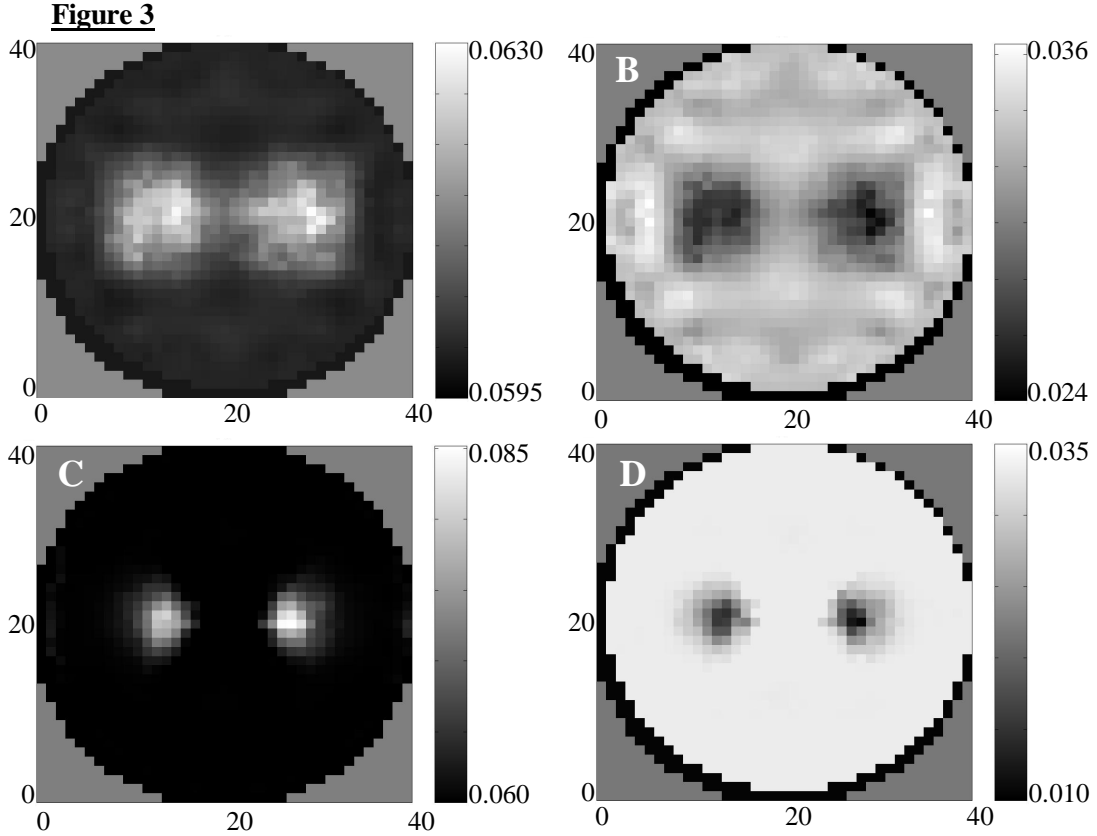
3. RESULTS

The mean values of the one thousand reconstructed images of μ_a and D are shown, for both reconstruction algorithm variants employed, in Figure 3. In Figure 4 we further examine the qualitative reconstruction accuracy by showing 1-D sections through the twentieth (*i.e.*, central) row of pixels, which bisects both inclusions, for the target medium (triangle symbols) and for the images of μ_a reconstructed, from the 101st set of detector data, by both the normalized difference (circle symbols) and the normalized-constraint CGD methods (square symbols). For ease of comparison, all curves have been rescaled to range from 0 to +1 in this Figure. From these it is evident that normalized-constraint CGD method yields significantly better spatial resolution in the result, and comparison of the grey scales in Figure 3 suggests that it also is producing a quantitatively more accurate answer.

As a demonstration of the applicability of correlation analysis to time series of optical coefficients, the correlation between the reconstructed and modeled μ_a time series was computed for a single pixel within each of the inclusions. When applied to the images reconstructed by the normalized difference CGD method, the result was $\rho(l) = 0.693$, $\rho(r) = 0.692$. From these we get $100\rho^2(l) = 48.0\%$, $100\rho^2(r) = 47.9\%$. That is, only somewhat less than half of the variability in the reconstructed μ_a time series in these pixels are linearly attributable to the variability that actually was present in the absorption coefficient at the same locations in the target medium. When the correlations between each pixel's time series of reconstructed μ_a and the modeled D in the same location were computed, the result was $\rho(l) = 0.722$ ($100\rho^2(l) = 52.2\%$), $\rho(r) = 0.718$ ($100\rho^2(r) = 51.6\%$). These values imply that the *apparent* absorption coefficient reconstructed by the normalized difference method in reality essentially is a 50/50 mixture of the target medium's μ_a and D . This is the worst-case scenario for inter-parameter cross-talk. (If, hypothetically, we had obtained a $\mu_a(t)^{\text{image}}$ vs. $\mu_a(t)^{\text{target}}$ ρ^2 of significantly less than 0.5 and a $\mu_a(t)^{\text{image}}$ vs. $D(t)^{\text{target}}$ ρ^2 of significantly greater than 0.5, then for the purpose of analyzing the dynamic properties of the optical coefficients we could simply relabel the D images as μ_a , and vice versa.)

The presence of maximal cross-talk is explicitly shown in Figure 5, where for each of the two pixels considered in this example the reconstructed $\mu_a(t)$ is plotted against the modeled $\mu_a(t)$ and $D(t)$. Each point in these scatter plots corresponds to one point in the time series. In each case the points define a plane. When both modeled parameters are taken into account

simultaneously, the overall correlations are $\rho(l) = 0.997$ ($100\rho^2(l) = 99.5\%$), $\rho(r) = 0.993$ ($100\rho^2(r) = 98.6\%$). This indicates that essentially all of the variability in the reconstructed $\mu_a(t)^{\text{image}}$ is attributable to a linear combination of $\mu_a(t)^{\text{target}}$ and $D(t)^{\text{target}}$. More extensive analysis shows that no significant increase in the overall correlation is achieved by including either nonlinear terms or the remaining two modeled optical coefficients as independent variables. In each Panel of Figure 5, two of the edges of the planes on which the plotted points lie are highlighted. The nearly equal contributions of modeled $\mu_a(t)^{\text{target}}$ and $D(t)^{\text{target}}$ to $\mu_a(t)^{\text{image}}$ is evidenced by the fact that both highlighted edges of these planes intersect the vertical coordinate planes at about the same height above the horizontal coordinate plane.

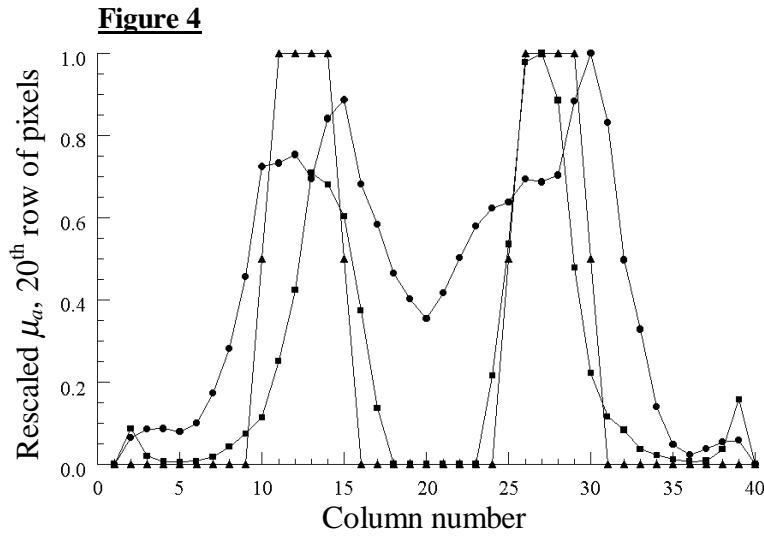


Legend Averages of 1000 reconstructed images of μ_a (Panels A and C) and of D (Panels B and D) of the dynamic target medium sketched in Figure 1. Results in Panels A and B were obtained when the normalized difference CGD method was used for reconstruction, while those in Panels C and D were obtained when the normalized–constraint CGD algorithm was used instead.

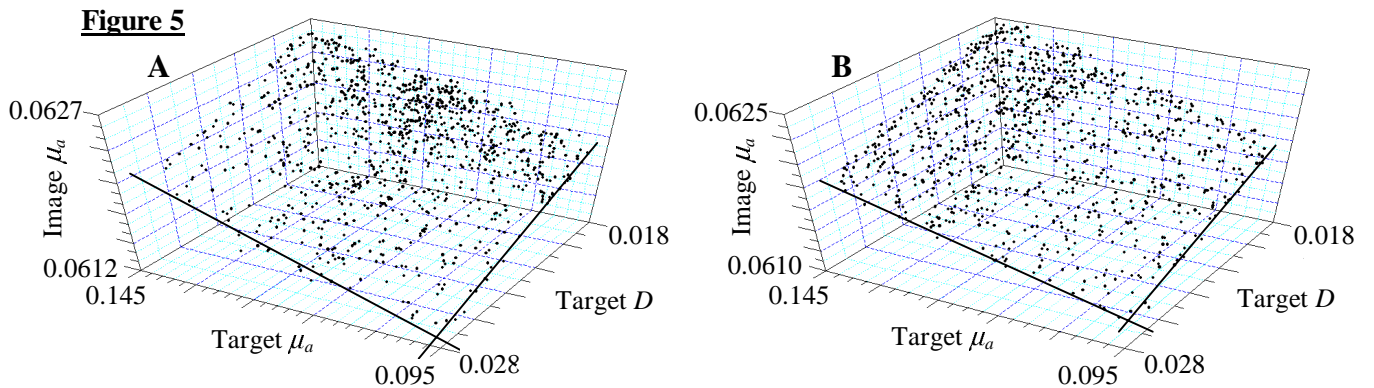
The same correlation analyses were applied to the time series of μ_a images reconstructed by the normalized–constraint CGD algorithm. In this case the computed $\mu_a(t)^{\text{image}}$ vs. $\mu_a(t)^{\text{target}}$ correlations were $\rho(l) = 0.945$, $\rho(r) = 0.936$ ($100\rho^2(l) = 89.4\%$, $100\rho^2(r) = 87.7\%$), while the μ_a^{image} vs. $D(t)^{\text{target}}$ correlations were $\rho(l) = 0.327$, $\rho(r) = 0.354$ ($100\rho^2(l) = 10.7\%$, $100\rho^2(r) = 12.5\%$). This shift to an approximately 90/10 split indicates that the improved reconstruction method achieves significant reductions in inter–parameter cross–talk, in addition to the already–noted improved spatial resolution. In Figure 6 we show recovered $\mu_a(t)$ vs. modeled $\mu_a(t)$ vs. modeled $D(t)$ scatterplots, for the same two pixels as in Figure 5, but using the results produced by the normalized–constraint CGD algorithm. It is seen in Figure 6 that each set of points defines a plane, two edges of which are highlighted. Note that, in contrast to the case for Figure 5, these edges intersect the vertical coordinate planes at significantly different heights above the horizontal coordinate plane. In particular, the edges that run along the “Target D ” axes rise more slowly than do the edges running along the “Target μ_a ” axes. This behavior is a significantly better approximation to the ideal result (*i.e.*, $\mu_a(t)^{\text{image}}$ independent of $D(t)^{\text{target}}$) than is that in Figure 5.

The results shown in Figure 6 further demonstrate that the introduction of constraints and weight–matrix scaling does not introduce appreciable nonlinearity into the relation between the target and medium properties. Neither do they produce any

dependence of the reconstructed coefficients in either inclusion on the properties that were present, in the target medium, in the other inclusion.



Legend One-dimensional sections through μ_a images reconstructed from 101st set of detector readings, by the CGD-only (circles) algorithm and constrained/rescaled CGD algorithm (squares). Also shown (triangles) is the corresponding section through the target medium. Curves have been rescaled to range from 0 to +1.



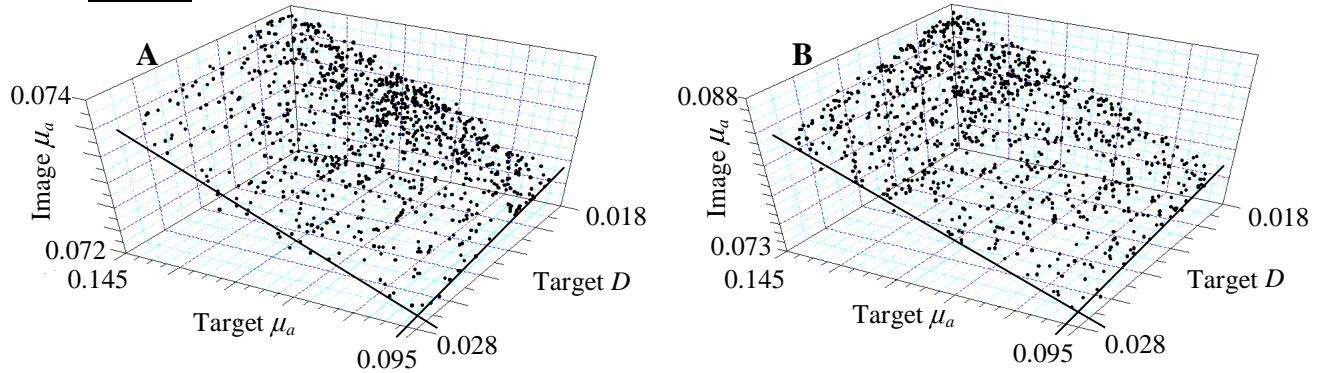
Legend Plots of reconstructed μ_a vs. modeled μ_a and D , for a selected pixel in the left-hand (Panel A) and right-hand (Panel B) inclusions, CGD-only algorithm. Each plotted point corresponds to a different time-point in the simulation time series. The surface defined by each set of plotted points is nearly planar.

In Figures 7 we show, for the results reconstructed by the normalized difference method, maps of the covariance between $\mu_a(t)^{\text{image}}$ and each of the four modeled functions $\mu_a(l,t)$, $D(l,t)$, $\mu_a(r,t)$, and $D(r,t)$. The results in Figures 7A and 7B indicate that both $\mu_a(l,t)$ and $\mu_a(r,t)$, reproduced in the image time series, are spatially accurate. However, the data presented in Figures 7C and 7D show that $\mu_a(t)^{\text{image}}$ actually is a combination of $\mu_a(l,t)$ and $D(l,t)$ throughout the area of the left-hand inclusion, and of $\mu_a(r,t)$ and $D(r,t)$ throughout the area of the right-hand inclusion. Note that the ranges displayed on the grey scales of all four Panels are of the same size. This indicates, as did the results of the correlation analysis applied to individual pixels, that both time-varying functions present in each inclusion make approximately equal contributions to $\mu_a(t)^{\text{image}}$.

Analogous covariance maps, computed from the $\mu_a(t)$ reconstructed by the normalized constraint CGD method, are shown in Figure 8. Previously it was shown (see Figure 3) that this algorithm recovers the *static* properties of the target medium with greater spatial resolution than the CGD-only method does. Here we see (Figures 8A and 8B) that normalized constraint method also recovers the *dynamic* properties of the inclusions' absorption coefficients with better spatial accuracy. The maps shown in Figures 8C and 8D indicate that inter-parameter cross-talk is not altogether eliminated by this algorithm.

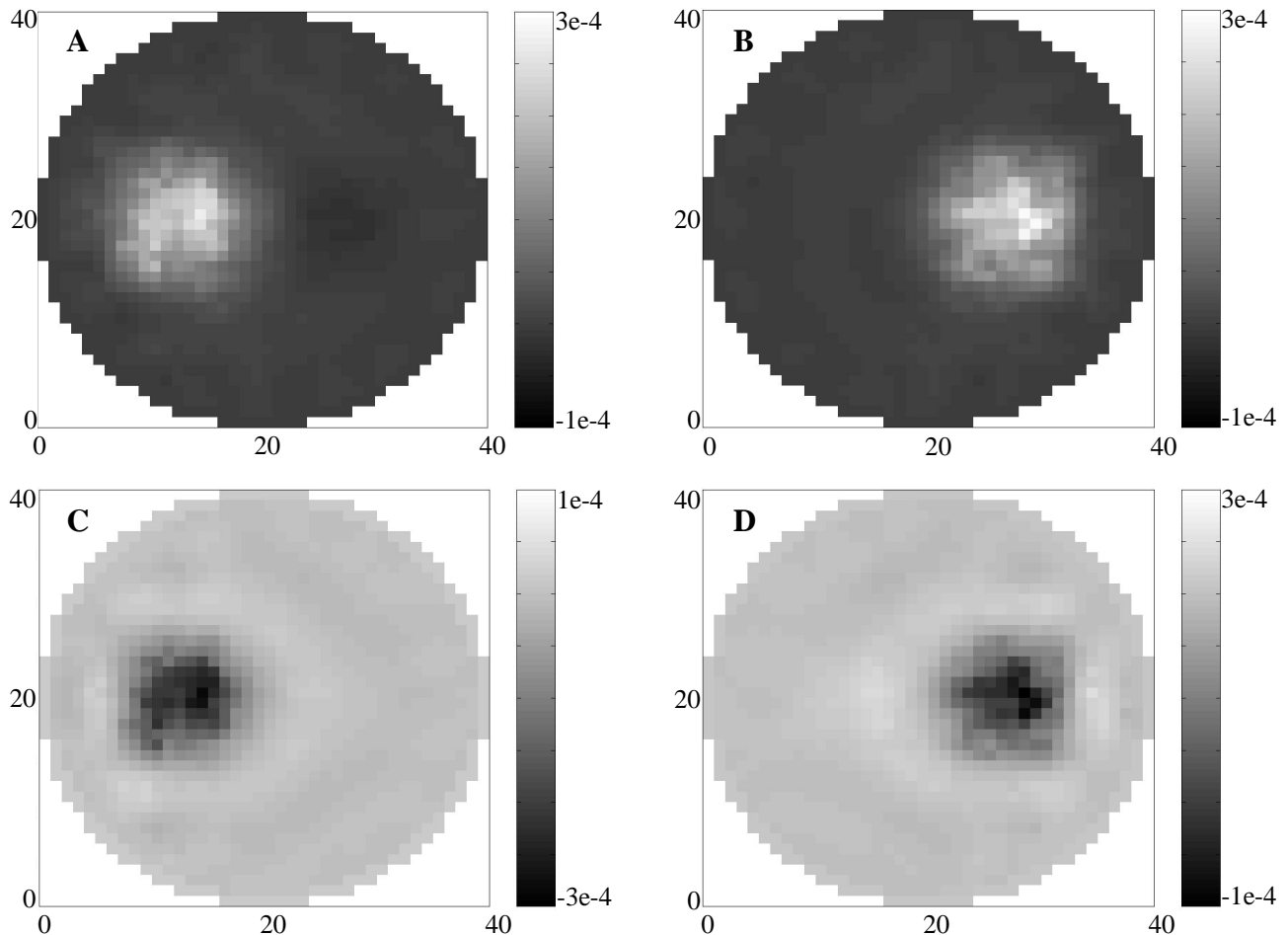
However, when the grey levels in Figure 8C(D) are contrasted with those in Figure 8A(B), it is apparent that the greatest (in absolute value) covariance between $\mu_a(t)$ and either $D(l,t)$ or $D(r,t)$ is significantly smaller than that between $\mu_a(t)$ and either $\mu_a(l,t)$ or $\mu_a(r,t)$. This is a qualitatively better result than that of Figure 7, in which the $\mu_a(t)^{\text{image}}$ vs. $D(t)^{\text{target}}$ cross-talk covariance is of the same magnitude as the $\mu_a(t)^{\text{image}}$ vs. $\mu_a(t)^{\text{target}}$.

Figure 6



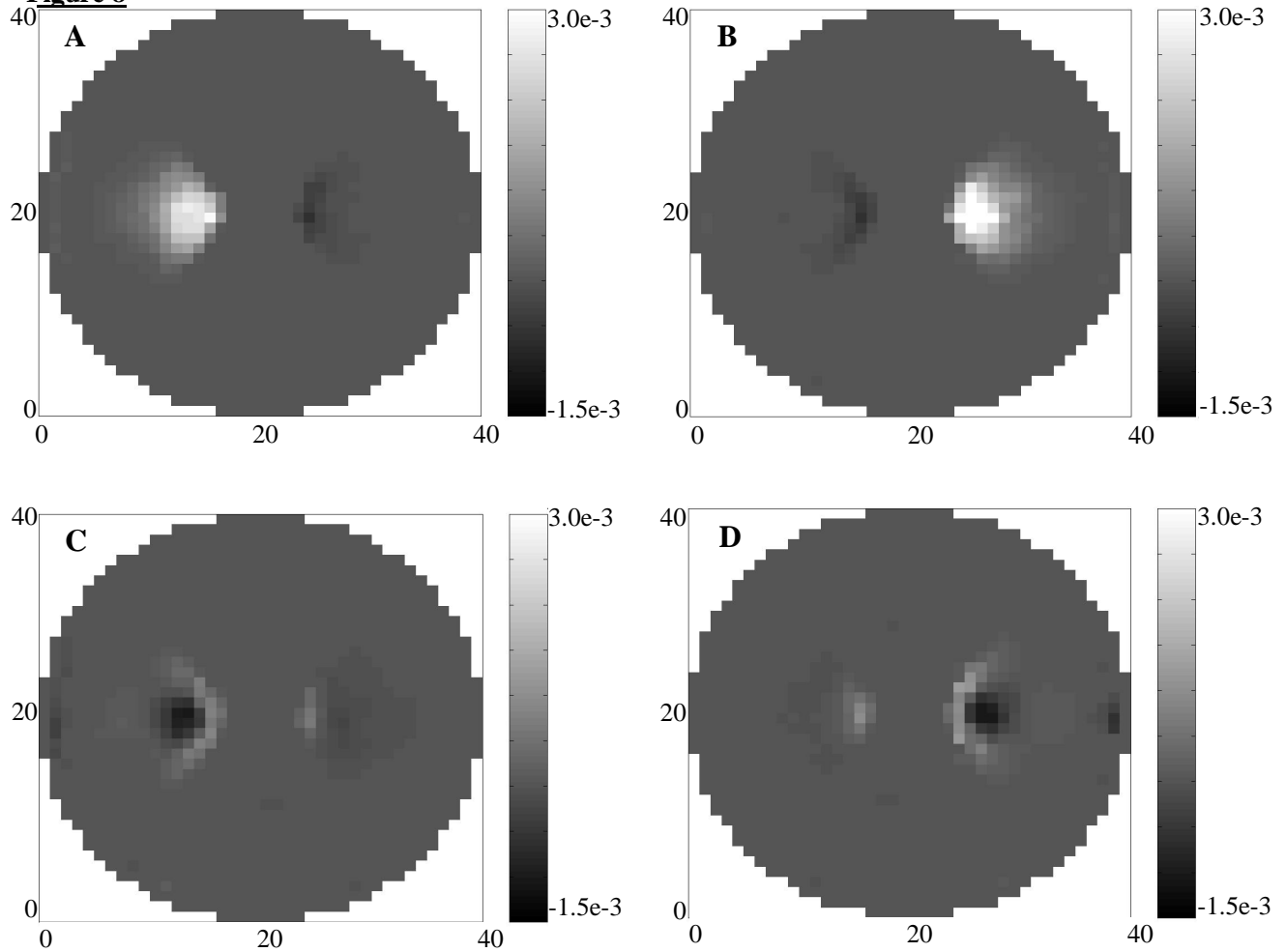
Legend Plots of reconstructed μ_a vs. modeled μ_a and D , for a selected pixel in the left-hand (Panel A) and right-hand (Panel B) inclusions, constrained/rescaled CGD algorithm. Each plotted point corresponds to a different time-point in the simulation time series. The surface defined by each set of plotted points is nearly planar.

Figure 7



Legend Maps of covariance, in each pixel, between the μ_a image time series reconstructed by the CGD-only algorithm and each of the four temporal fluctuations that were present in the target medium. Plotted are covariances between reconstructed μ_a^{image} and: Panel A, $\mu_a(l,t)$; Panel B, $\mu_a(r,t)$; Panel C, $D(l,t)$; Panel D, $D(r,t)$.

Figure 8



Legend Maps of covariance, in each pixel, between the μ_a image time series reconstructed by the constrained/rescaled CGD algorithm and each of the four temporal fluctuations that were present in the target medium. Plotted are covariances between reconstructed μ_a and: Panel A, $\mu_a(l,t)$; Panel B, $\mu_a(r,t)$; Panel C, $D(l,t)$; Panel D, $D(r,t)$.

A small degree of spatial cross-talk between the inclusions is evident in the results shown in figure 8. This is not an artifact introduced by the reconstruction method. Close examination of the corresponding results in Figure 7 show that the same phenomenon is present in the CGD-only results, but is distributed over a larger area. This, and the greater variability in covariance values found in the background region in the absence of constraints, renders the spatial cross-talk in the grey-scale images presented in Figure 7 less noticeable than that in Figure 8.

The results presented in Figures 7 and 8 also indicate that the two pixels selected for the detailed correlation analysis presented above are representative, in terms of the temporal properties of their reconstructed $\mu_a(t)$, of the two inclusions.

Finally, while space limitations have led us to explicitly present results comparing only the reconstructed $\mu_a(t)$ to the temporal properties of the target medium, the corresponding analyses involving the reconstructed D time series also have been performed. The constrained/rescaled CGD algorithm yielded qualitatively superior $D(t)$ reconstructions than the CGD-only algorithm, of the same magnitude as those presented above for $\mu_a(t)$, in terms of both spatial resolution and inter-parameter cross-talk.

4. DISCUSSION AND CONCLUSIONS

Delineation of contrast mechanisms is important to any imaging modality. In optical tomography, naturally occurring contrast features include the spatially-varying absorption and scattering properties of tissue. Whereas numerical reconstruction methods have been developed that are capable of simultaneously solving for both coefficients, inter-parameter cross-talk not infrequently occurs. This refers to the situation wherein a perturbation in one coefficient (*e.g.*, absorption) can influence the computed value of the other (*e.g.*, scattering) and vice versa. Results presented in this report add to the evidence presented in the accompanying study by Pei *et al.*,² who described a new algorithm for minimizing parameter cross-talk using DC imaging data. Here we have considered the limiting case wherein the temporal variations in the optical properties of one parameter (*e.g.*, absorption) are both spatially and temporally coincident with those of another (*e.g.*, scattering). Clearly demonstrated was the finding that the different test functions can be effectively isolated, irrespective of their functional form, or of the instantaneous value of the ratio of absorption to scatter. These findings do not support the assertion by Arridge and Lionheart,¹⁵ who claim that such separation is not possible using DC imaging data.

The current capabilities add to those enumerated in a series of accompanying reports wherein we describe instrumentation¹ and numerical methods¹⁶ that we have adopted for the collection and analysis of time-series image data. These methods represent various components of a more inclusive methodology we seek to apply for the characterization of the spatiotemporal properties of vascular reactivity in large tissues using near infrared optical imaging methods. It is our belief that such measures performed on tissue either at rest or in response to some homeostatic provocation, represents a large untapped reservoir for identifying new diagnostic measures of disease processes, as well as for monitoring the influence of a host of therapeutic regimens.

Optical imaging methods hold the promise of enabling the visualization of a range of functional properties of tissue that are not detectable using other imaging technologies. Its inherent sensitivity to hemoglobin, use of nonionizing energy sources, deep penetrating power in tissue, capacity to employ low-cost portable instrumentation, and recently, the added capability of monitoring dynamic states, all serve to underscore the expanding utility of this technology.

5. ACKNOWLEDGMENT

This research was supported by NIH grant RO1-CA 66184.

6. REFERENCES

1. C. H. Schmitz, M. Löcker, J. Lasker, A. H. Hielscher, and R. L. Barbour, "Performance characteristics of a silicon photodiode (SiPD) based instrument for fast functional optical tomography," Proc. SPIE Vol. 4250 (2001, accompanying report).
2. Y. Pei, H. L. Graber, and R. L. Barbour, "Normalized-constraint method for minimizing inter-parameter cross-talk in reconstructed images of spatially heterogeneous scattering and absorption coefficients," Proc. SPIE Vol. 4250 (2001, accompanying report).
3. R. L. Barbour, H. L. Graber, C. H. Schmitz, Y. Pei, S. Zhong, S.-L. S. Barbour, S. Blattman, and T. Panetta, "Spatiotemporal imaging of vascular reactivity by optical tomography," *Proceedings of Inter-Institute Workshop on In Vivo Optical Imaging at the NIH*, A. H. Gandjbakhche, Ed. (Optical Society of America, Washington, DC 2000), pp. 161-166. (Presented at the National Institutes of Health, Bethesda, MD, Sept. 16-17, 1999).
4. H. L. Graber, C. H. Schmitz, Y. Pei, S. Zhong, S.-L. S. Barbour, S. Blattman, T. Panetta, R. L. Barbour, "Spatio-Temporal Imaging of Vascular Reactivity," in *Medical Imaging 2000: Physiology and Function from Multidimensional Images*, C.-T. Chen, A. V. Clough, Eds., Proceedings of SPIE Vol. 3978, pp. 364-376 (2000).
5. C. H. Schmitz, H. L. Graber, H. Luo, I. Arif, J. Hira, Yaling Pei, A. Bluestone, S. Zhong, R. Andronica, I. Soller, N. Ramirez, S.-L. S. Barbour, R. L. Barbour, "Instrumentation and calibration protocol for imaging dynamic features in dense-scattering media by optical tomography," *Applied Optics* **39**, 6466-6486 (2000).
6. R. L. Barbour, H. L. Graber, Y. Pei, S. Zhong, and C. H. Schmitz, "Optical tomographic imaging of dynamic features of dense-scattering media," *J. Opt. Soc. Am. A* (2001), in press.
7. L. Glass and M. C. Mackey, *From Clocks to Chaos: The Rhythms of Life* (Princeton University Press, Princeton, NJ 1998).
8. T. M. Griffith, "Chaos and fractals in vascular biology," *Vascular Medicine Review* **5**, 161-182 (1994).
9. M. C. Mackey and L. Glass, "Oscillation and chaos in physiological control systems," *Science* **197**, 287-289 (1977).
10. A. H. Nayfeh and B. Balachandran, *Applied Nonlinear Dynamics: Analytical, Computational, and Experimental Methods* (John Wiley & Sons, New York, 1995), Chap. 4.

11. K. Briggs, "An improved method for estimating Liapunov exponents of chaotic time series," *Physics Letters A* **151**, 27–32 (1990).
12. Y. Pei, F.-B. Lin, and R. L. Barbour, "Modeling of sensitivity and resolution to an included object in homogeneous scattering media and in MRI-derived breast maps," *Optics Express* **5**, 203–219 (1999).
13. Y. Pei, "Optical Tomographic Imaging Using Finite Element Method," Ph.D. Dissertation, Polytechnic University, Brooklyn, NY, 1999.
14. Ref. 10, Chap. 7.
15. S. R. Arridge and W. R. B. Lionheart, "Nonuniqueness in diffusion-based optical tomography," *Optic Letters* **23**, 882–884 (1998).
16. G. Landis, S. Blattman, T. Panetta, C. H. Schmitz, H. L. Graber, Y. Pei, and R. L. Barbour, "Clinical applications of dynamic optical tomography in vascular disease," Proc. SPIE 4250 (2001, accompanying report).